



ELSEVIER

Available online at www.sciencedirect.com

SCIENCE @ DIRECT®

**NUCLEAR
INSTRUMENTS
& METHODS
IN PHYSICS
RESEARCH**
Section A

www.elsevier.com/locate/nima

Nuclear Instruments and Methods in Physics Research A 524 (2004) 195–207

The silicon matrix as a charge detector in the ATIC experiment

V.I. Zatsepin^{a,*}, J.H. Adams^b, H.S. Ahn^c, G.L. Bashindzhagyan^d, K.E. Batkov^a,
J. Chang^f, M. Christl^b, A.R. Fazely^e, O. Ganel^e, R.M. Gunasingha^e, T.G. Guzik^d,
J. Isbert^d, K.C. Kim^c, E.N. Kouznetsov^a, M.I. Panasyuk^a, A.D. Panov^a,
W.K.H. Schmidt^f, E.S. Seo^c, N.V. Sokolskaya^a, J.Z. Wang^c, J.P. Wefel^d, J. Wu^c

^aSkobel'syn Institute of Nuclear Physics, Moscow State University, Vorobyevy Gory, Moscow 119899, Russia

^bMarshall Space Flight Center, Huntsville, AL, USA

^cUniversity of Maryland, College Park, MD, USA

^dLouisiana State University, Baton Rouge, LA, USA

^eSouthern University, Baton Rouge, LA, USA

^fMax Plank Institute fur Aeronomie, Lindau, Germany

Received 24 July 2003; received in revised form 19 January 2004; accepted 30 January 2004

Abstract

The Advanced Thin Ionization Calorimeter (ATIC) was built for series of long-duration balloon flights in Antarctica. Its main goal is to measure energy spectra of cosmic ray nuclei from protons up to iron nuclei over a wide energy range from 30 GeV up to 100 TeV. The ATIC balloon experiment had its first, test flight that lasted for 16 days from 28 December 2000 to 13 January 2001 around the continent. The ATIC spectrometer consists of a fully active BGO calorimeter, scintillator hodoscopes and a silicon matrix. The silicon matrix, consisting of 4480 pixels, was used as a charge detector in the experiment. About 25 million cosmic ray events were detected during the flight. In the paper, the charge spectrum obtained with the silicon matrix is analyzed.

© 2004 Elsevier B.V. All rights reserved.

PACS: 96.40.De; 95.55.Vj; 29.40.Wk

Keywords: Cosmic rays; Charge composition; Charge detector; Silicon matrix

1. Introduction

The power-law energy spectrum of primary cosmic rays continues on up to energy of 10^{20} eV. The only bright feature of this spectrum is the well-known 'knee' around 10^{15} eV. The nature of this knee is still unknown, in spite of numerous

attempts, undertaken with indirect methods. Direct particle-by-particle measurements, with good charge resolution, of elemental energy spectra are necessary to resolve the astrophysical questions. One possible explanation of the knee is the cessation of particle acceleration at a rigidity of 10^{14} V, that is predicted by the most popular acceleration model: acceleration in the expanding shells of supernova remnants [1]. If so, the ATIC experiment's data may come rather close, for the proton component, to this critical rigidity.

*Corresponding author. Tel.: +95-939-3808; fax: +95-939-3553.

E-mail address: viza@dec1.sinp.msu.ru (V.I. Zatsepin).

Another necessity for accurate measurements in the region below 100 TeV is the situation concerning the proton spectrum in the energy region near 1 TeV. In the experiments executed during 1965–1968 on board the PROTON satellite [2], it was stated that the spectral index increases from $\gamma = 1.6$ at energy below 0.5 TeV to the value of 2.1 above 2 TeV. Charge measurements in the experiment were performed by non-sectioned scintillator detectors of large area. These results were not convincing because of possible distortion of the measured charge by albedo particles from the calorimeter.

The albedo problem was solved, in principle, in the SOKOL experiment, where directional Cherenkov detectors were used for measuring the proton and helium charge. However, high energy threshold (2–5 TeV) and lack of statistics did not allow SOKOL to clarify the situation. The team which carried out the experiment was not able to come to the agreement on the experiment results [3,4].

The JACEE emulsion chamber experiments did not find a steeper spectrum above 1 TeV [5]; the spectrum agreed with lower energy data. In the Moscow University Balloon Emulsion Experiment MUBEE [6] the conclusion was that the slope of proton integral spectrum at energy above 10 TeV is $\gamma = 2.14 \pm 0.08$ in disagreement with the early JACEE results. Further balloon flights by JACEE refined the spectrum above 10 TeV, finding a continuous spectrum with an integral spectral index $\gamma = 1.80 \pm 0.04$ in the entire energy region [7]. The same result $\gamma = 1.78 \pm 0.05$ was obtained in the RUNJOB experiment [8].

The ATIC experiment is a new attempt to resolve these issues. It aims to study elemental charge composition and energy spectra of the primary cosmic rays in the energy region from 30 GeV up to 100 TeV.

2. Scheme of the ATIC spectrometer

The ATIC spectrometer consists of three main parts: charge module, carbon target and calorimeter (see Fig. 1) In the experiment, the events selected are those in which a primary particle

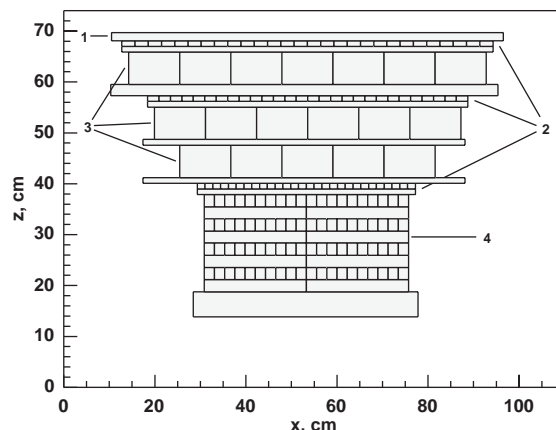


Fig. 1. Schematic view of the ATIC spectrometer: 1—silicon matrix, 2—scintillator hodoscopes, 3—carbon target, 4—BGO calorimeter.

passes through the charge module, interacts in the carbon target, and generates an electron–hadron cascade in the calorimeter. The charge is measured by a matrix of silicon detectors. The target module consists of three layers of carbon each 10 cm thick and three hodoscopes of plastic scintillators with a cross section of $2 \times 1 \text{ cm}^2$ and lengths of 88.2, 74.2 and 52.4 cm for the upper, middle and lower hodoscope, respectively. Each hodoscope consists of two planes of strips oriented at the angle of 90° . They form the first level triggers, determining the aperture of the instrument, and provide additional measurements of charge and trajectory of the primary particle or the cascade. The fully active calorimeter consists of 320 crystals of bismuth germanate (BGO) $25 \text{ cm} \times 2.5 \text{ cm} \times 2.5 \text{ cm}$ in size arranged in eight layers alternately along the x - and y -axis. The ATIC configuration and operation are described in more detail in Refs. [9–11].

3. Silicon matrix

The matrix of silicon detectors, used in the ATIC experiment for primary particle identification, consists of 4480 silicon pixels arranged in four planes. The active detector areas in these planes have a slight overlap to cover completely the ATIC aperture. The basic element of the

matrix is a daughterboard on which a four-pixel silicon detector is mounted. The detector consists of four separate pixels, produced on one silicon strip. Twenty eight daughterboards are mounted on a motherboard, which is a multilayer circuit board 109 cm long and 6.634 cm wide that also carries the front-end electronics for the detectors. Two motherboards located one above the other ‘face to face’ and shifted so that the active areas are partially overlapped, form a structure termed a ladder. The matrix has two panels of ladders with 10 ladder in each. These panels are mounted with a shift, so that the active areas of the upper and lower ladders also partially overlap (see Fig. 2). The active area of the matrix is 99.2 cm \times 111.2 cm, i.e. 11031 cm². The sum of active areas of all pixels is 12852 cm², the difference accounted

for by overlap. The four-pixel detectors are made on wafers of super-pure silicon 10 cm in diameter and 380 μ m thick produced by Wacker Siltronic, Germany. The active area of the detector pixel is 1.945 \times 1.475 cm², so that the whole detector has an active area of 1.945 \times 5.9 cm². These detectors are PIN diodes with a sharp p–n junction. A common contact is created on one side by phosphorus diffusion, while the individual detector pixels are produced on the other side by boron ion implantation. The nominal capacitance of each detector pixel is 90 pF. The full depletion voltage for the selected detectors is <80 V, while the operation voltage is 100 V. The selected detectors are mounted on ceramic boards. The manufacturing techniques for the detectors are stated in more detail in Ref. [12].

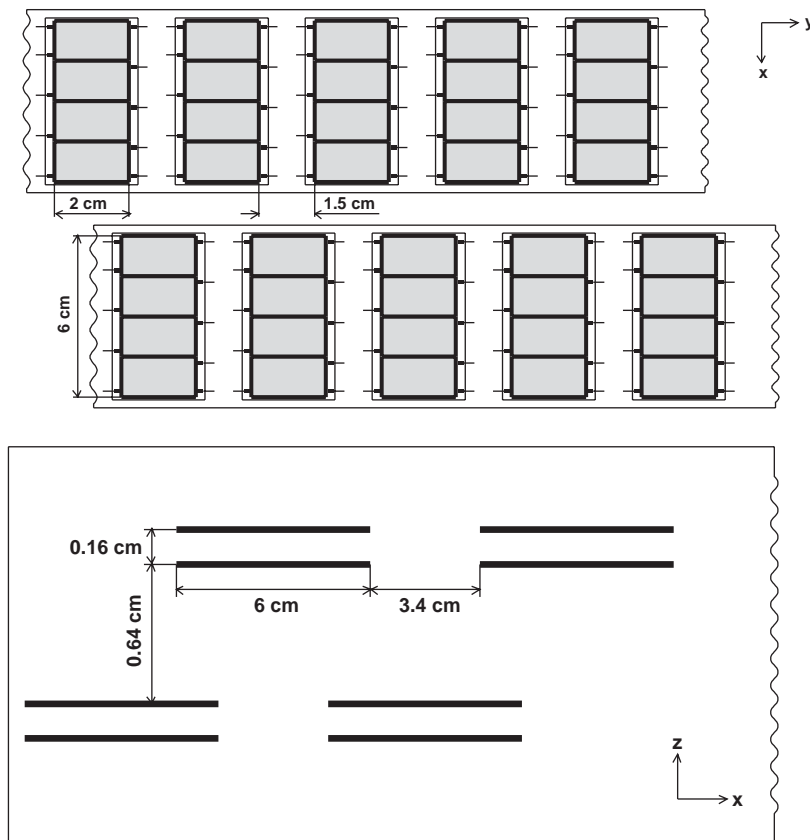


Fig. 2. Scheme of the silicon matrix. Top panel: two motherboards that make up a ladder; the top motherboard is inverted and placed over the bottom motherboard so that the detectors are offset by half a pitch. The detectors are spaced so that they slightly overlap within the ladder. Bottom panel: location of ladders in the silicon matrix (side view). Neighboring ladders slightly overlap each other.

4. Reconstruction of event trajectories

The first step in the analysis is trajectory reconstruction from the BGO-calorimeter. The trajectory is described by two projections in the plains XZ and YZ. Both projections are reconstructed independently using Y-oriented and X-oriented layers of crystals, respectively. The energy deposit E_i in the layer i is checked, and if $E_i < 50$ MeV, then the event is not considered.

The crystal with the maximal energy deposit in a layer is determined. If this crystal is found near the edge of the layer, the event is considered to be a ‘side event’ and is ignored. Then the ‘symmetrized’ center of weight of the energy distribution in the layer is obtained. From GEANT simulation [13], for an energy deposit in layer E_i , the dispersion σ of the weight center is obtained. Then, a trajectory is calculated by minimization of χ^2 value. This BGO trajectory is projected up to the intersection with the Si-matrix plane, and an area of $\pm 3\sigma$ in each coordinate is determined. For each silicon pixel with non-zero signal inside the ‘area of search’ the trajectory is traced through the center of this pixel and weight centers in the calorimeter layers. For each trajectory, the existence of signals in all six scintillators along this trajectory is checked. The selection of such ‘confirmed’ trajectories suppresses noise signals in the silicon matrix. Finally, for the confirmed trajectories the Si pixel with maximal signal is selected, and primary particle charge is determined by: $Z = \sqrt{A \times \cos \Theta}$, where A is signal in the silicon pixel in mip’s and Θ is the zenith angle defined by this trajectory. The value of mip is energy deposit of minimal ionizing particle in a silicon pixel.

5. Adjusting silicon pixel response

In the ATIC experiment, elemental charge resolution is the goal. To obtain this resolution in the real experiment, it is necessary to bring the signals, measured in each pixel to a unified scale, that is to correct for different gains in different electronic channels and differences in thickness of silicon in the pixels. At a first step, the response was adjusted with pre-flight muon calibration.

However, this calibration was not exact enough, because of lack of statistics in each pixel.

5.1. ‘Helium adjusting’

After the first stage, lines of H, He, C and O were seen, and lines of Ne, Mg, Si and S were not well resolved. To improve the calibration, the flight data location of the Helium peak in each pixel was used. As a measure of this location, the mean value of signals during the flight in the range from 2 to 8 mip was used. This mean value was normalized to the calculated value of energy deposition obtained by simulation with the GEANT code. The charge spectrum after ‘helium adjusting’ became better. The lines of B, Ne, Mg, Si and S were visible. The results obtained from this step were published in Ref. [14].

The ‘helium adjusting’ had in mind that two conditions were fulfilled: (1) the Si-matrix electronics was stable during the entire flight and (2) the pulse characteristics of all electronic channels were linear. The first condition appeared to be true. The stability of the instrument operating was controlled during the entire flight with hour measurements of pulse characteristics for all electronic channels. For example, in Fig. 3a typical time dependence of a channel response is shown for one

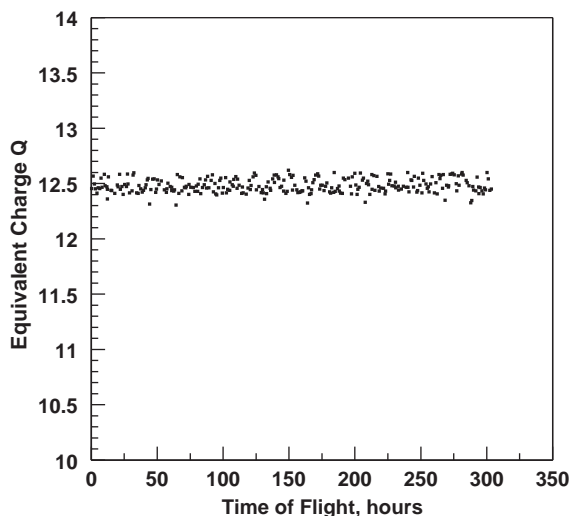


Fig. 3. Example of time dependence response of a channel to a calibration signal, $Q = \sqrt{A/A}$, mip.

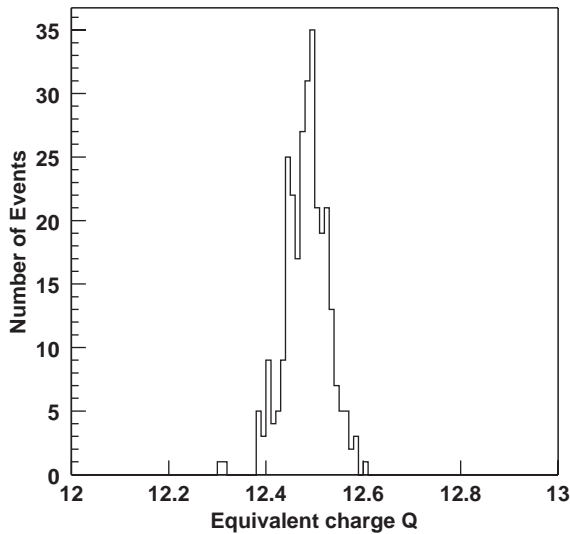


Fig. 4. Example of dispersion of time dependence response of a channel to a calibration signal, $Q = \sqrt{A/A}$, mip.

of 27 calibration signals. In Fig. 4 the pulse distribution of this response is shown. It is seen that the dispersion of output signal is about 0.04 charge units, and such a dispersion has little effect on the charge resolution. The second condition appeared not to be true. Both laboratory and in-flight measurements showed small non-linearities of the pulse characteristics, which are different for different channels. The most significant of these non-linearities were in the range of big charges: $Z > 20$. Further, we carried out the data corrections taking into account non-linearities for each channel in the entire range of pulses.

5.2. Electronic channel adjusting

During the total flight two types of calibration runs were executed periodically. One of them—measurement of individual channel pedestals—was done every 6 min, with the aim of automatic correction of the sparsification thresholds, and were stored for further data correction. Second a calibration was executed every hour and was also stored for post-flight data correction. As already said, this calibration contains the full amplitude calibration of each channel using a set of 27 test pulse amplitudes settings from 0.3 mip up to 1700

mip. In doing so, the pulse from the calibration generator was put through the flight test pulse line to 112 channels on each motherboard simultaneously. This strategy had, however, some disadvantages:

- (1) The common pulse that was put to the test pulse line did not deliver the same charge to each channel due to both differences in the real capacities, through which the charge is delivered from the common bus to the individual channels, and cross talk in the front-end electronics.
- (2) The flight test line had high capacity. So, for high amplitude input pulses, the output pulse transmitted was non-linear.

To eliminate these weaknesses of the method, each channel was calibrated in the laboratory with the same probe capacitor, through which test pulses were put from a calibrated generator to each channel. In this case, each channel obtained the same charge. A comparison of these pulse characteristics with the pulse characteristic obtained with the flight test line allows us to calculate a correction factor for each channel.

The full plan for the flight data correction was the following:

- (1) The pedestals were subtracted from the raw data to obtain pure pulses in channels. The pedestal values were updated every 6 min.
- (2) For these pulses, the signals that were put from the flight calibration generator were determined by the flight calibration curve.
- (3) To obtain the real charge, the non-linearity of the flight test line was corrected (using the laboratory calibration with probe capacitor).

This method allowed to update the flight calibrations, which were measured every hour, but the weak dependence from temperature and narrow range of temperature variance during the flight made these updates not necessary.

A typical example of non-linearity of pulse characteristics measured in a flight calibration run is shown in Fig. 5. The relative channel gain is on the y -axis and pulse amplitude that was input by the flight calibration generator is on the x -axis.

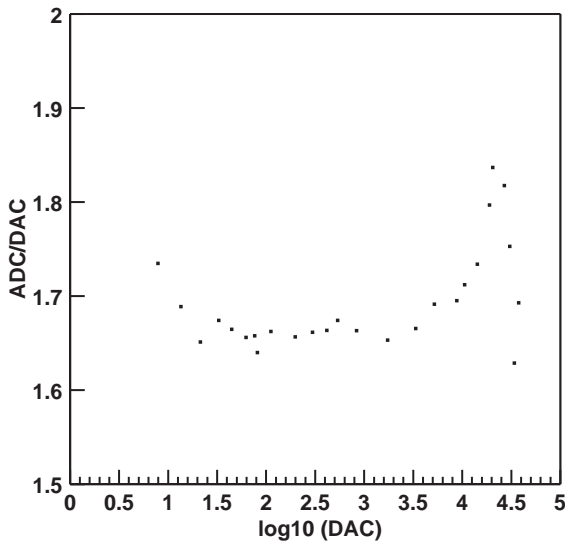


Fig. 5. Non-linearity of a channel response obtained by the in-flight calibration.

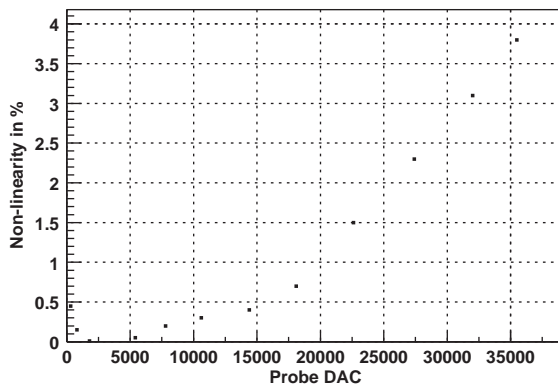


Fig. 6. Non-linearity of the flight generator obtained with a probe generator.

Fig. 6 shows a typical non-linearity for the flight test line. Significant non-linearity of pulse characteristics of CR-1 chips (16-channel amplifiers used for reading out signals from silicon detectors) exists only for pulses higher than 300 mip (> 10000 ADC channels), that is why the preliminary analysis for the region < 300 mip was done in the linear approximation. The flight data were processed both in the linear approximation and using the full procedure taking into account the non-linearity. In the latter case, two values $lcut$

and $hcut$ were determined for pulse characteristics of each channel. These values divided the pulse characteristic into three ranges: low, middle and high. A linear interpolation was used in the low range, and the interpolation with polynomial of third degree was used for the middle and high ranges. So, 12 parameters were used to correct the non-linearity of each channel's pulse characteristics from the flight calibration. In the same way, a second step of correction was done—determination of real pulse by correction of non-linearity of the flight test line. So, for correction of measured pulse, 24 parameters were determined for each of 4480 electronic channels of the silicon matrix.

6. Results and analysis

The results on charge distribution obtained with the full correction method are shown in Fig. 7 for protons and helium nuclei and in Fig. 8 for other nuclei. Let us first consider the situation in the group of light nuclei. It is well known that backscattered particles can distort the signal produced by the primary particle in the charge detector. The main problem while measuring the charge of protons and helium nuclei in the highly segmented silicon matrix consists in finding the pixel which was crossed by the primary particle. This problem is connected with the accuracy of trajectory reconstruction in the thin calorimeter. In the search area with a side of 3σ in each coordinate, there can be a few pixels with pulses above sparsification thresholds from noise or from backscattered particles. To reject noise, confirmation in the scintillators along trajectory traced through the given pixel and weight centers in the calorimeter was required. Among such pixels, the pixel with maximal signal was chosen.

Although the accuracy of trajectory reconstruction increases with increasing energy deposition in the calorimeter, the density of albedo increases also. Therefore, charge resolution in the group of protons and helium could depend on energy. The obtained resolution is shown in Fig. 7 for three energy ranges: > 10 , > 100 and > 1000 GeV. One can see that protons and helium are separated reasonably well for the entire energy range.

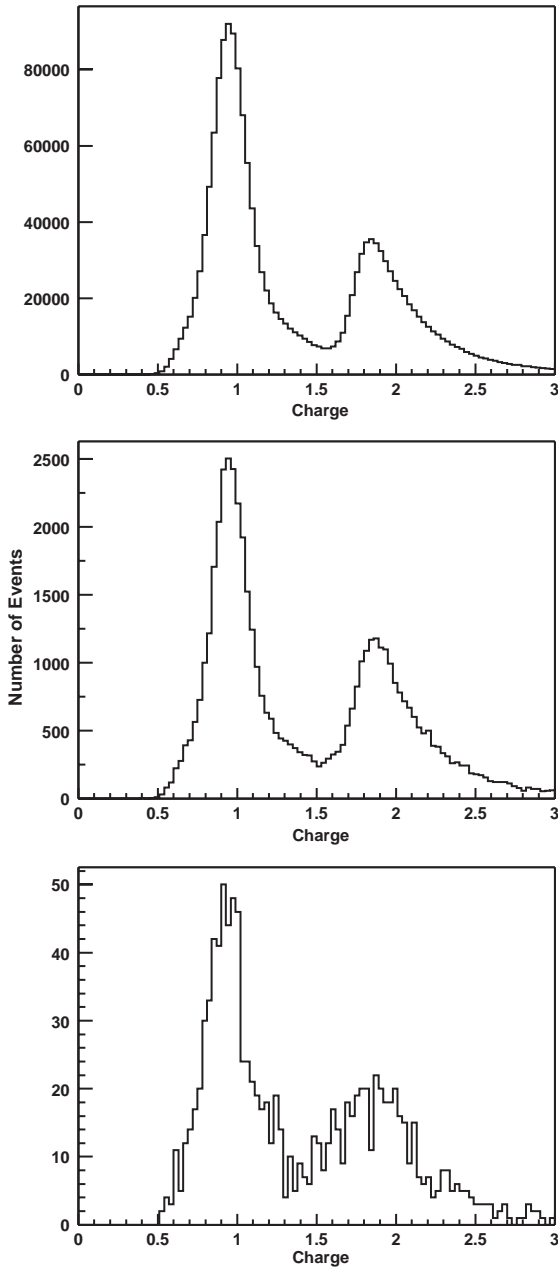


Fig. 7. Charge resolution for protons and helium; top panel: $E_d > 10$ GeV, middle panel: $E_d > 100$ GeV, bottom panel: $E_d > 1000$ GeV.

An investigation of the effect of albedo showed that albedo signals of about 1 mip dominate in the silicon matrix. The probability of albedo signals

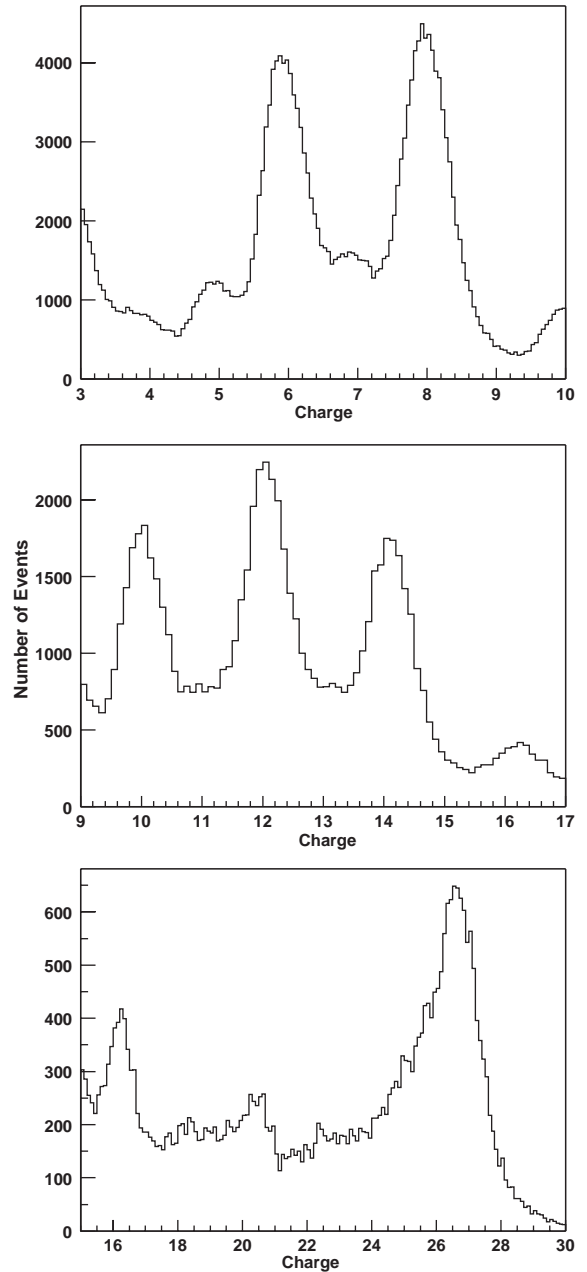


Fig. 8. Charge resolution for three regions of charge.

decreases exponentially with increasing signal size. Therefore, albedo cannot distort significantly the measured signal in the case of a nucleus heavier than helium. For nuclei with $Z > 5$, a pixel crossed

Table 1
Comparison of different methods of charge measurement correction in the silicon matrix

Method	Nucleus					
	C	O	Ne	Mg	Si	Fe
1	0.32	0.33	0.44	0.41	0.49	—
2	0.30	0.31	0.37	0.39	0.39	0.59
3	0.32	0.31	0.32	0.36	0.37	0.47
4	0.23	0.23	0.23	0.23	0.23	0.26

1. Adjusting by He peak. 2. Channel gain correction in the linear approximation. 3. Channel gain correction taking into account non-linearity. 4. Expected results from simulation before the experiment. The values show widths of Gaussian distributions σ in charge units

by the primary particle is determined practically unambiguously. For those nuclei, an accuracy of pixel adjusting is more essential.

The different methods of charge measurement correction in the silicon matrix are compared in Table 1. The values in the table show widths of Gaussian distributions σ in charge units. The first row shows the results of adjusting by He peak. The second and third rows are for channel gain corrections in the linear approximation and taking into account non-linearity, respectively. The fourth row shows the expected results for the silicon matrix from simulation before the experiment [15].

For calculations of σ values in Table 1, the fact was used that the silicon matrix was designed with overlapping of silicon pixels. For vertical direction this overlapping is about 15% of the area. The events were selected in which maximal signal in the search area was followed by a signal in an overlapping pixel. These two signals were marked throughout their height in the matrix: QSiUp and QSiDn for the top and bottom pixel correspondingly. The distributions of the value (QSiUp–QSiDn) were approximated with Gaussian functions and the values of σ were determined as $\sigma(\text{QSiUp} - \text{QSiDn})/\sqrt{2}$, as illustrated in Fig. 9. We can make the following conclusions from Table 1: (a) in the region of middle nuclei all three methods lead to the same results, and (b) for nuclei heavier than oxygen, taking into account the non-linearity of the pulse characteristics of the electronic

channels leads to the significant improvement of charge resolution (especially for iron nuclei).

In a previous paper [15], it was assumed that the width of charge peaks (in units of charge) can be described by the expression

$$\sigma_Z = Z/2 \times \sqrt{(\delta_{\text{ion}}/Z)^2 + (\delta_{\text{noise}}/Z)^2 + (\delta_t)^2}, \quad (1)$$

where δ 's are relative dispersions of signal for singly charged particle due to ionization loss, noise in the detectors and electronics and thickness variations of the detector within one pixel. The expected values of the parameters were the following: $\delta_{\text{ion}} = 0.44$, $\delta_{\text{noise}} = 0.05$ and $\delta_t = 0.01$. The expected values of σ shown in fourth line of Table 1 was obtained with these values of the dispersions. Analysis of Table 1 shows that:

- The role of fluctuations of ionization loss is higher in the real silicon matrix, since the expected resolution was not achieved for the middle nuclei.
- The fluctuations which do not depend on pulse height (third term in Eq. (1)) also are higher, because the peak widths increase with Z for $Z > 10$.

6.1. Fluctuations of ionization losses

In Ref. [15] the contribution of ionization loss fluctuations in Eq. (1) was described with the value of $\delta_{\text{ion}} = 0.44$. This value was obtained by simulation of passing nucleus with charge Z through a silicon pixel not taking into account material above the silicon pixel. However, in fact there is a printed circuit board (≈ 2 mm of fiberglass) or printed circuit board plus ceramic plate of 0.7 mm above the detectors. Table 2 shows the influence of material surrounding the detector on mean value and dispersion of proton and helium signals for energy of 100 GeV. The simulation was done with GEANT-4 code [16]. One can see from the table, that surrounding material increases both the mean value of energy deposit (about 8%) and dispersion (about 1.42 times) for both protons and helium. It is seen also that the increasing ends at thickness of fiberglass over 2 mm. Fig. 10 shows simulated

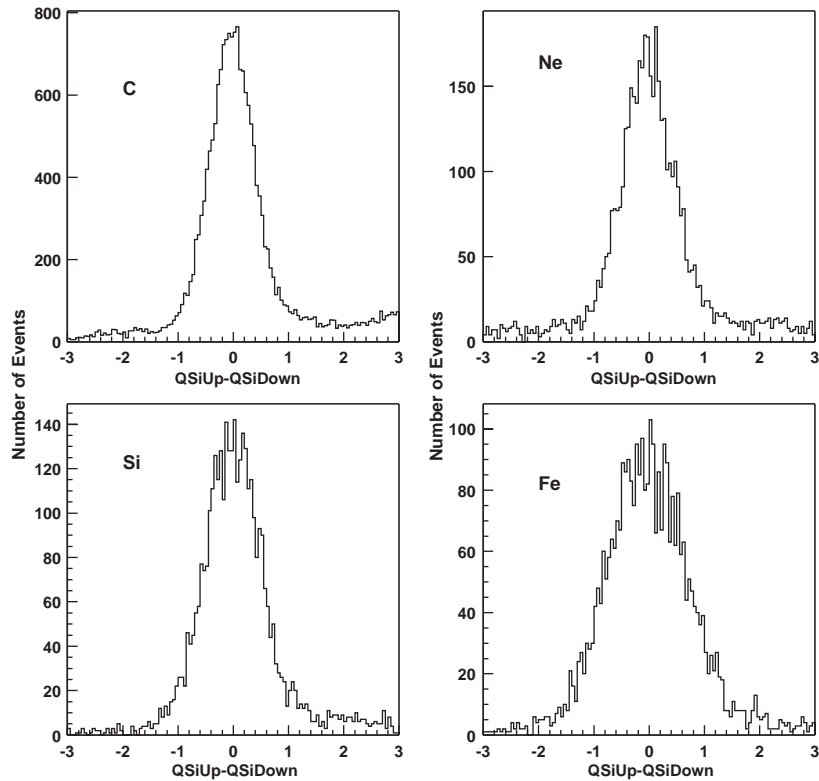


Fig. 9. Distribution of (QSiUp–QSiDown) for C, Ne, Si and Fe nuclei.

Table 2

Influence of material surrounding a silicon pixel on mean value $\langle E \rangle$, dispersion σ_{ion} and relative dispersion $\sigma_{\text{ion}}/\langle E \rangle$, of 100 GeV's proton and helium energy deposition in the silicon pixel

Fiberglass thickness (mm)	Protons			Helium		
	$\langle E \rangle$ (keV)	σ_{ion} (keV)	$\sigma_{\text{ion}}/\langle E \rangle$	$\langle E \rangle$ (keV)	σ_{ion} (keV)	$\sigma_{\text{ion}}/\langle E \rangle$
0	134.6	57.48	0.427	530.7	117.1	0.220
0.5	139.1	71.15	0.511	551.0	144.4	0.262
1.0	143.7	82.85	0.576	560.4	157.9	0.281
2.0	146.1	90.14	0.617	574.0	177.2	0.309
4.0	147.4	90.37	0.613	585.2	188.5	0.322

charge distribution for CNO nuclei in case of bare silicon detector and for a silicon detector which is surrounded with 2 mm of fiberglass. One can see that the simulation with surrounding material describes the experimental situation in the ATIC silicon matrix quite well. So, in fact the value of δ_{ion} in Eq. (1) should be 0.61.

6.2. Effect of noises

Let us now consider the influence of noises. The value of $\delta_{\text{noise}} = 0.05$ was obtained in Ref. [15] in laboratory measurements as intrinsic noise of the main bulk of the silicon detectors. The total value of noise includes also noise in the flight electronics.

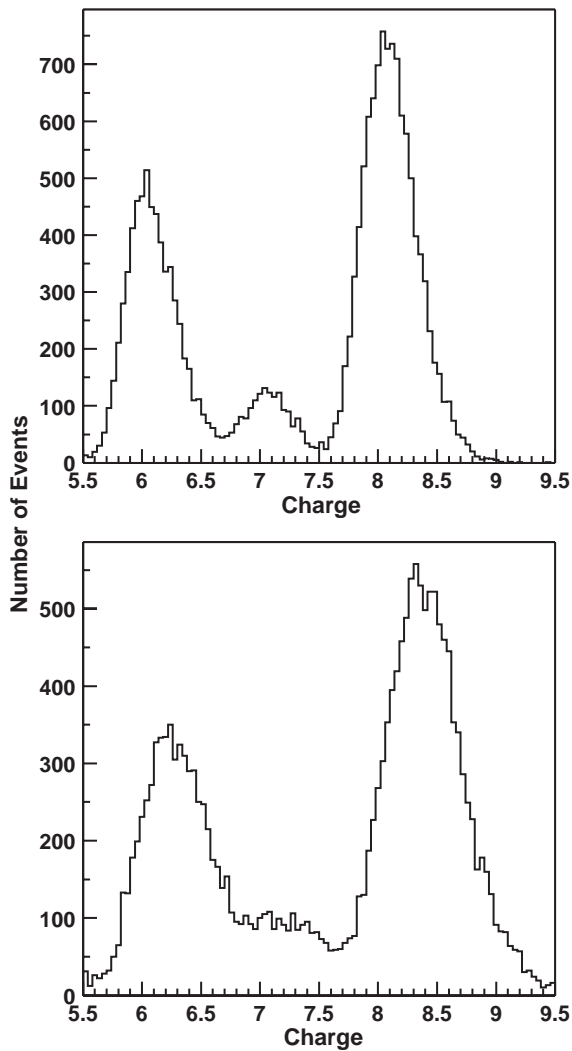


Fig. 10. Simulated charge distribution for CNO group. Top panel: without material, bottom panel: with 2 mm of fiberglass.

The noises for all electronic channels were measured in the calibration runs during the flight. Two typical examples are shown in Fig. 11. The value of $\text{rms}(A_{\text{out}})/A_{\text{in}}$ in % is on the y -axis and value of A_{in} is on the x -axis, where A_{out} and A_{in} are output and input pulse amplitudes. The value of A_{in} for a mip is near 20th channel of digital-analog converter (DAC), and it was found that the noise of the flight electronics is about eight times larger than the intrinsic noise of the silicon detectors. The average value of $\delta_{\text{noise}} \approx 0.4$. But in spite of this,

noise of the front-end electronics is significant only for the light nuclei ($Z \leq 4$). However, it was found that there were two groups of channels, approximately equal in quantity, with different behavior of noise at high DAC amplitude: channels with normal noises (Fig. 11, left panel) and channels with noises that were independent on the input pulse above $A > 3000$ channels of DAC, i.e. > 150 mip (Fig. 11, right panel). The value of this noise is equal to 2.5–3%. If such noise was not only in the calibration runs, but also in the flight events, this might explain the poorer resolution for nuclei of $Z > 12$. To check if such noise was present in the flight events, we again turn to the events of iron group, detected in the two-layer matrix. All these events were divided into two groups: the first group consisted of events measured in channels with low noises both in upper and lower pixels ($\delta_{\text{noise}}/A < 1\%$), while events detected in channels with high noise in one or both pixels comprised the second group. The results are the following: the value of σ for the first group is 0.465 ± 0.0012 , being 0.507 ± 0.010 for the second group. So, the increase of σ from the expected value of 0.32 up to 0.47 is governed by another reason.

6.3. Effect of detector thickness dispersion

The measured width of iron peak might be due to dispersion of thickness of the silicon wafer disks from which the detectors were produced. According to data from the wafer producer, this dispersion is $\pm 15 \mu\text{m}$ ($\approx 4\%$). This value might be enough to explain the observed resolution for $Z > 10$, if it converts directly to the width of the Gaussian distribution. But, such dispersion might be corrected by adjusting signals for the Fe-peak. The mean value of Fe-peak position was calculated for each four-pad detector, which was produced from one wafer. Fig. 12 shows the charge distribution in the charge interval $20 < Z < 30$ before and after the adjusting. We do not see any noticeable improvement.

To describe the Fe-peak width, the value of δ_t would need to be equal to 0.027. It seems likely that this value is according to the remainder of the noise after the gain non-linearity correction and the detector thickness correction.

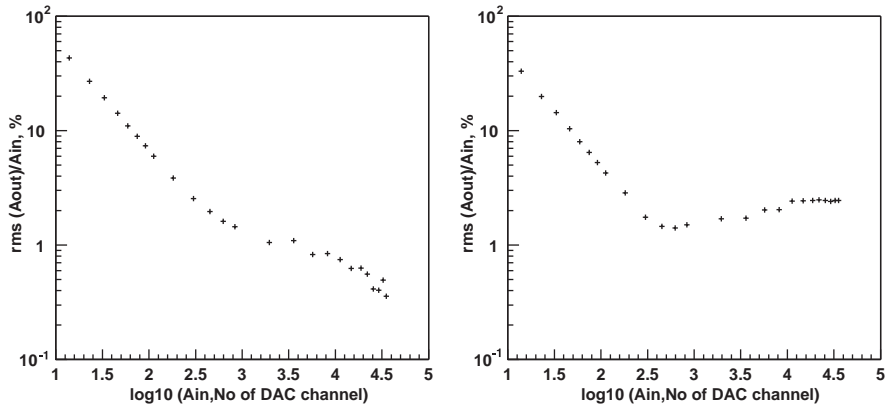


Fig. 11. Noises; left panel: low noise channel, right panel: high noise channel.

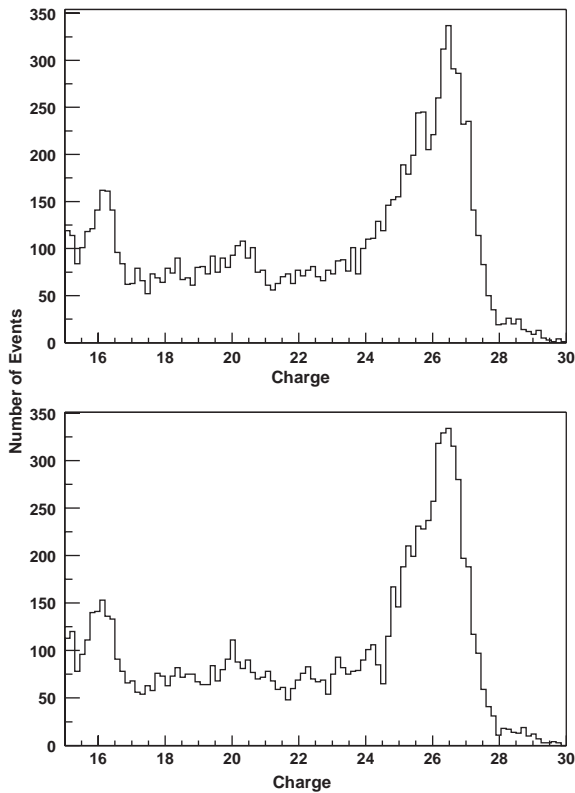


Fig. 12. Charge resolution; top panel: low noise channels, bottom panel: low noise channels after calibration with Fe.

So, the charge resolution obtained in the first flight of ATIC may be described by Eq. (1) with the following parameters: $\delta_{\text{ion}} = 0.61$, $\delta_{\text{noise}} = 0.40$ and $\delta_t = 0.027$.

7. Charge resolution of two-layer matrix

For events which were detected in the overlapping areas of the pixels we were able to obtain charge resolution in a ‘two-layer matrix’. We applied the following algorithm:

1. As usual, the cascade trajectory was traced to the silicon matrix and the pixel with maximal value of signal Q_{max} was found in the area of search of $\pm 3\sigma$ for both x and y coordinate.
2. The following intervals were set for Q_{max} , where different nuclei should be detected: $0.5 < Q_{\text{max}} < 1.7$ for protons; $1.7 < Q_{\text{max}} < 2.7$ for helium; $2.7 < Q_{\text{max}} < 3.5$ for Li; $3.5 < Q_{\text{max}} < 4.5$ for Be; $4.5 < Q_{\text{max}} < 5.5$ for B and so on up to $27.5 < Q_{\text{max}} < 28.5$ for Ni.
3. The presence of second signal was required in the overlapping pixels with Q_2 value being between Q_{max} and the left boundary of the charge interval, predetermined for the nuclei with type determined by Q_{max} .
4. The mean value $Q_{\text{mean}} = (Q_{\text{max}} + Q_2)/2$ was used to construct the charge distribution for the two-layer matrix.

The charge resolution obtained for the two-layer matrix is shown in Fig. 13. Statistics in the two-layer matrix is about 8% of the total.

One can see that good resolution of all neighboring elements has been achieved in this case. The analysis of reliability of the results for the two-layer matrix is in progress.

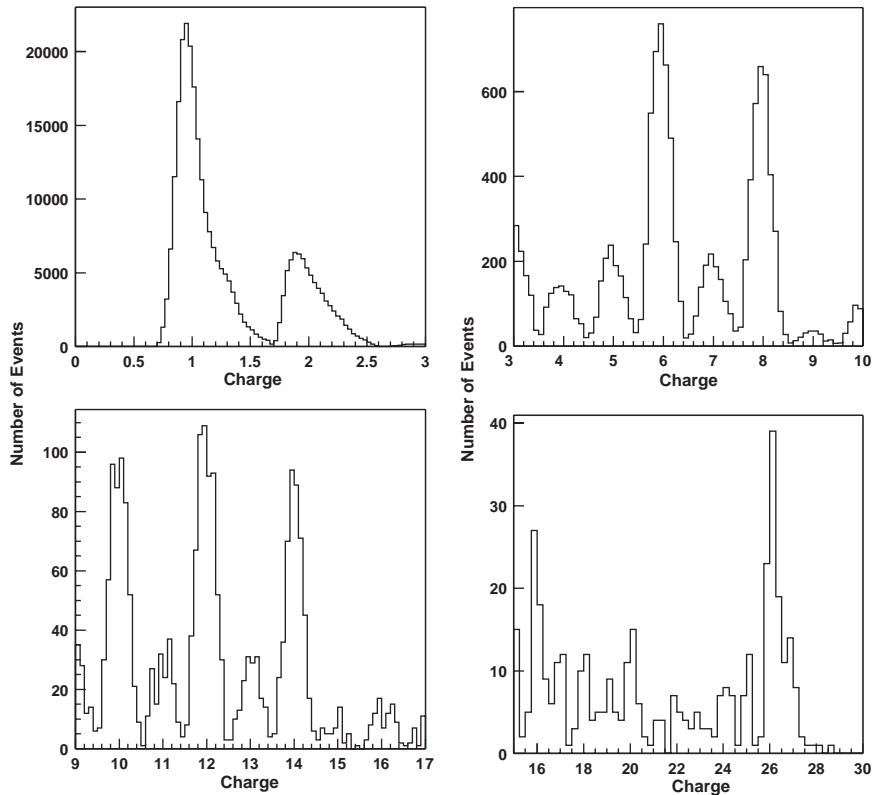


Fig. 13. Charge resolution of the two-layer Si matrix.

8. Conclusion

The analysis of charge resolution obtained in the silicon matrix in the first flight of the ATIC spectrometer showed the following:

1. Protons and helium nuclei are reliably separated in the energy region from 30 GeV to 10 TeV. Backscattered particles do not distort, noticeably, the charge measured in the silicon matrix in this energy region.
2. The main groups of nuclei (CNO, Ne–S and Fe) are completely separated, the more abundant even nuclei (C, O, Ne, Mg, Si and S) produce clearly visible peaks on the charge spectrum.
3. The Fe nuclei form a clearly defined peak.
4. The accuracy of corrections for non-linear gains of the electronic channels and for thickness of the silicon detectors is not adequate to obtain complete elemental resolution for nuclei of $Z >$

10. The existence of structural material close to the silicon detectors precludes complete elemental resolution for light and medium nuclear.
5. The application of a silicon matrix with two layers of silicon detectors provides complete elemental resolution over the total charge range.

Acknowledgements

This work was supported with NASA grants to LSU, MSFC, UMD and SU. In Russia the work is supported by Russian Foundation for Basic Research, Grant 02-02-16545.

References

- [1] T.K. Gaisser, *Cosmic Rays and Particle Physics*, Cambridge University Press, Cambridge, 1990.

- [2] N.L. Grigorov, G.P. Kakhidze, I.D. Rapoport, et al., *Kosmicheskie issledovaniya* 5 (1967) 38 (in Russian);
N.L. Grigorov, N.A. Mamontova, I.D. Rapoport, et al., Proceedings of the 12th International Cosmic Ray Conference, Vol. 5, Tasmania, 1971, p. 1752.
- [3] N.L. Grigorov, *Sov. J. Nucl. Phys.* 51 (1990) 99;
N.L. Grigorov, *Yad. Fiz.* 51 (1990) 157.
- [4] I.P. Ivanenko, V.Ya. Shestoporov, L.O. Chikova, et al., Proceedings of the 23rd International Cosmic Ray Conference, Vol. 2, Calgary, 1993, p. 17.
- [5] T.H. Burnett, S. Dake, M. Fuki, et al., *Phys. Rev. Lett.* 52 (1983) 1010.
- [6] V.I. Zatsepin, E.A. Zamchalova, A.Ya. Varkovitskaya, et al., Proceedings of the 23rd International Cosmic Ray Conference, Vol. 2, Calgary, 1993, p. 13.
- [7] K. Asakimory, T.H. Burnett, M.L. Cherry, et al., *Astrophys. J.* 502 (1998) 278.
- [8] A.V. Apanasenko, V.A. Sukhadolskaya, V.A. Derbina, et al., *Astropart. Phys.* 16 (2001) 13.
- [9] E.S. Seo, J.H. Adams, G.L. Bashindzhagyan, et al., *Adv. Space Res.* 19 (1997) 711.
- [10] T.G. Guzik for The ATIC Collaboration, Proceedings of the 26th International Cosmic Ray Conference, Vol. 5, Salt Lake City, 1999, p. 9.
- [11] J.P. Wefel for The ATIC Collaboration, Proceedings of the 27th International Cosmic Ray Conference, Vol. 6, Hamburg, 2001, p. 2111.
- [12] N.V. Baranova, G.L. Bashindzhagyan, A.G. Voronin, et al., Silicon detectors for the hadron–electron separator for ZEUS experiment DESY, preprint NPI MSU - 95-43/407, Moscow, 1995 (in Russian).
- [13] R. Brun, F. Brayant, M. Maire, GEANT Users Manual, CERN DD/EE/84-1, Geneva, 1984.
- [14] V.I. Zatsepin, J.H. Adams Jr., H.C. Ahn, et al., *Izv. Ross. Akad. Nauk.* 66 (2002) 1634.
- [15] J.H. Adams Jr., G.L. Bashindzhagyan, V.I. Zatsepin, et al., *Instrum. Exp. Tech.* 44 (4) (2001) 455.
- [16] S. Agostinelli, J. Allison, K. Amako, et al., *Nucl. Instr. and Meth. A* 506 (2003) 250.